REPORT DOCUMENTION PAGE

Public reporting burden for this collection of information is estimated to average 1 hour per response, including the time for reviewing instructions, searching existing data sources, gathering and maintaining the data needed, and completing and reviewing the collection of information. Send comments regarding this burden estimate or any other aspect of this collection of information, including suggestions for reducing this burden, to Washington Headquarters Services, Directorate for Information Operations and Reports, 1215 Jefferson Davis Highway, Suite 1204, Arlington, VA 22202-4302, and to the Office of Management and Budget, Paperwork Reduction Project (0704-0188), Washington, DC 20503.

1. AGENCY USE ONLY *(Leave blank)*	2. REPORT DATE 29 July 99	3. REPORT TYPE AND DATES COVERED Final; 01 Aug 98 – 30 Apr 99

4. TITLE AND SUBTITLE Object Oriented PIC Code with Upgraded Physics and Platform Independent GUI	5. FUNDING NUMBERS F49620-98-C-0053

6. AUTHOR(S)

David Bruhwiler, John Verboncoeur and Kelly Luetkemeyer

19990803 084

7. PERFORMING ORGANIZATION NAME(S) AND ADDRESS(ES) Tech-X Corporation, 1280 28th Street, Suite 2 Boulder, CO 80303 University of California, 336 Sproul Hall Berkeley, CA 94720	8. PERFORMING ORGANIZATION REPORT NUMBER STTR99 FINAL

9. SPONSORING/MONITORING AGENCY NAME(S) AND ADDRESS(ES) Dr. Arje Nachman Air Force Office of Scientific Research 801 N. Randolph Street, Room 732 Arlington, VA 22203	10. SPONSORING/MONITORING AGENCY REPORT NUMBER

11. SUPPLEMENTARY NOTES

12a. DISTRIBUTION/AVAILABILITY STATEMENT Distribution Statement A; Approved for public release; distribution is unlimited	12b. DISTRIBUTION CODE

13. ABSTRACT *(Maximum 200 words)*   The relativistic radiation damping and accompanying electron self-force is, in principle, properly modeled by the standard PIC (particle-in-cell) algorithm; however, due to grid resolution and time step constraints, there is no possibility of directly simulating the fields of the emitted radiation over a spectrum sufficient to include a significant fraction of the radiated power, so a scheme has been developed to correct for these errors. A model for secondary emission of electrons from arbitrary surfaces with user definable coefficients has been developed and implemented in the XOOPIC (X11-based Object-Oriented Particle-In-Cell) code, allowing for separate secondary emission treatment of each species incident on each boundary. A literature survey determined the four algorithms most relevant to treating electromagnetic boundary conditions in a PIC model, along with their respective strengths and weaknesses. The errors in the generic PIC algorithm have been analyzed in the electrostatic limit, and an initial extension of this analysis to the generic electromagnetic PIC scheme was developed. A large subset of the existing XOOPIC GUI, which runs only under Unix, has been ported to a new cross-platform windowing library, called Qt, that runs equally well on Microsoft Windows 95/98/NT and all versions of Unix.

14. SUBJECT TERMS particle-in-cell, high-power microwave electron self-force, secondary electron emission		15. NUMBER OF PAGES 15
		16. PRICE CODE

17. SECURITY CLASSIFICATION OF REPORT UNCLASSIFIED	18. SECURITY CLASSIFICATION OF THIS PAGE UNCLASSIFIED	19. SECURITY CLASSIFICATION OF ABSTRACT UNCLASSIFIED	20. LIMITATION OF ABSTRACT SAR

NSN 7540-01-280-5500

Tech-X Corporation

July 29, 1999

Final Report (August 1, 1998 - April 30, 1999)
STTR Phase I project, contract number F49620-98-C-0053
"Object-oriented PIC code with upgraded physics and platform-independent GUI"
David Bruhwiler, Principal Investigator;   (303) 448-0732, bruhwile@txcorp.com

Abstract

The relativistic radiation damping and accompanying electron self-force is, in principle, properly modeled by the standard PIC (particle-in-cell) algorithm; however, due to grid resolution and time step constraints, there is no possibility of directly simulating the fields of the emitted radiation over a spectrum sufficient to include a significant fraction of the radiated power, so a scheme has been developed to correct for these errors. A model for secondary emission of electrons from arbitrary surfaces with user definable coefficients has been developed and implemented in the XOOPIC (X11-based Object-Oriented Particle-In-Cell) code, allowing for separate secondary emission treatment of each species incident on each boundary. A literature survey determined the four algorithms most relevant to treating electromagnetic boundary conditions in a PIC model, along with their respective strengths and weaknesses. The errors in the generic PIC algorithm have been analyzed in the electrostatic limit, and an initial extension of this analysis to the generic electromagnetic PIC scheme was developed. A large subset of the existing XOOPIC GUI, which runs only under Unix, has been ported to a new cross-platform windowing library, called Qt, that runs equally well on Microsoft Windows 95/98/NT and all versions of Unix.

Modeling the Electron Self-Force

The relativistic electron self force is a physical process in which the acceleration of a relativistic electron causes the electron to radiate. The energy is negligible except for radiation from highly relativistic particles. A prototypical configuration that exhibits radiation damping is a relativistic electron in a strong magnetic field.

Jackson [1] derives the power radiated from a relativistic particle undergoing a strong acceleration in a uniform magnetic field:

$$P = \frac{2}{3} \frac{e^2 c}{4\pi\varepsilon_0 r_L^2} \beta^4 \gamma^4 ,$$

where e is the electronic charge, c is the speed of light, ε_0 is the permittivity of free space, $\beta = v/c$, and $\gamma = \left(1 - \beta^2\right)^{-1/2}$. The relativistic gyroradius is given by:

$$r_L = \frac{v}{\omega_c} = \frac{\gamma m \beta c}{eB} = \sqrt{\gamma^2 - 1}\, \frac{mc}{eB} , \qquad\qquad 1$$

where m is the electron mass and B is the magnetic field.

Tech-X Corporation

July 30, 1999

Defense Technical Information Center / OCP
8725 John J Kingman Road, Suite 0944
Fort Belvoir VA 22060-6218
(703) 767-8023

To whom it concerns,

I have enclosed two copies of the final report for the AFOSR Phase I STTR project
"Object Oriented PIC Code with Upgraded Physics and Platform Independent GUI",
contract # F49620-98-C-0053. This report covers the period from August 1, 1998 through
April 30, 1999.

This report has been accepted by the program manager, Dr. Arje Nachman.

Please let me know if you need any additional information.

Sincerely yours,

David Bruhwiler, Principal Investigator
(303) 448-0732
bruhwile@txcorp.com

The energy radiated by the electron per gyro-orbit is approximately:

$$\delta E \approx \frac{2\pi r_L}{\beta c} P = \frac{e^2}{3\varepsilon_0 r_L} \beta^3 \gamma^4.$$

2

The spectral content of the radiated power is a complicated function. Jackson derives the energy radiated per unit frequency per unit solid angle:

$$\frac{d^2 I}{d\omega d\Omega} = \frac{e^2}{3\pi^2 c} \left(\frac{\omega r_L}{c}\right)^2 \left(\frac{1}{\gamma^2} + \theta^2\right)^2 \left(K_{2/3}^2(\xi) + \frac{\theta^2}{1/\gamma^2 + \theta^2} K_{1/3}^2(\xi)\right).$$

3

Here, θ is the angle from the plane of circular motion, K is the modified Bessel function, and ξ is given by:

$$\xi = \frac{\omega r_L}{3c} \left(\frac{1}{\gamma^2} + \theta^2\right)^{3/2}.$$

4

The radiation is strongly polarized in the plane of motion, with increasing confinement to the plane of motion with increasing frequency. The radiation is negligible beyond the critical frequency,

$$\omega_{crit} = 3\gamma^3 \frac{c}{r_L}.$$

5

Another useful quantity is the critical harmonic number, $n_{crit} = 3\gamma^3$, which describes the number of significant harmonics present in the radiation spectrum for a particle undergoing a periodic motion such as synchrotron radiation.

Similarly, a critical angle beyond which the radiation drops to 1/e is given by:

$$\theta_c \approx \frac{1}{\gamma} \sqrt{\frac{\omega_c}{3\omega}}.$$

6

Equation 6 indicates that the radiated power is confined to increasingly smaller angles at higher frequencies, as well as with increasing particle energy. The radiation is emitted from a particle undergoing circular motion in a pattern similar to the sweep of a lighthouse beam, with the focus always centered in the direction of the velocity.

The relativistic radiation damping and accompanying self force is properly modeled by the coupled Maxwell and Newton-Lorentz Equations. However, in PIC simulation, the finite nature of the time- and space-steps results in error for this force. An example is useful in illustrating the difficulty in modeling this phenomena with the standard PIC method.

Consider a 1 GeV electron orbiting a 10 T static magnetic field. The relativistic momentum factor is $\gamma = 1952$, and the velocity is effectively the speed of light, c, to six places. The gyroradius is 0.334 m. The power radiated is $P = 6 \times 10^{-6}$ W, so the electron would lose 1% of its energy in about 270 ns. The critical frequency is $\omega_{crit}/2\pi = 3.2 \times 10^{18}$ Hz, with a corresponding critical wavelength of $\lambda_{crit} = 9.4 \times 10^{-11}$ m. In order to resolve the wavelength on

the mesh, we would need $\Delta x \le \lambda / 4 = 2.4 \times 10^{-11}$ m. For a nominal system length of $L = 3r_L$ in each dimension, the required number of cells in each dimension is 4.2×10^{10}, or 1.7×10^{21} cells in a two dimensional simulation. This exceeds the memory capacity of existing computers. Furthermore, the timestep required to satisfy the Courant condition is $\Delta t \le \Delta x / \sqrt{2} c = 5.7 \times 10^{-20}$ s. The cyclotron period is 7 ns, so one orbit would require 1.2×10^{11} timesteps, while running to 1% energy loss would require 4.7×10^{12} timesteps. Resolving the critical frequency requires a timestep $\Delta t \le 3.1 \times 10^{-19}$ s, which is even more untenable.

The conclusion to this analysis is that the radiation damping cannot be self-consistently modeled by the standard PIC scheme even for a single particle. Due to the grid resolution and timestep constraints, there is no possibility of directly simulating the fields of the radiation emitted over a spectrum sufficient to include a significant fraction of the radiated power.

To correct this problem, one can implement a modification to the equation of motion that will include the radiation damping term for the particle equations of motion:

$$F^{rad} = \frac{2}{3} \frac{e^2}{4 \pi \varepsilon_0 c^4} \frac{\gamma}{\sqrt{\gamma^2 - 1}} \left(\frac{d\mathbf{p}}{dt} \cdot \frac{d\mathbf{p}}{dt} \right),$$

7

where $\mathbf{p}$ is the particle momentum. The derivative must be time centered to maintain the second order accuracy of the equation of motion:

$$\frac{d\mathbf{p}}{dt} = \frac{\sqrt{\gamma^2 (t + \Delta t / 2) - 1} - \sqrt{\gamma^2 (t - \Delta t / 2) - 1}}{\Delta t} mc .$$

8

Note that the relativistic momenta are computed at the half timestep level in the standard PIC leapfrog mover, so this term maintains the existing accuracy of the method (see accuracy section below). The force is directed anti-parallel to the velocity of the electron.

If it is desired to follow the radiation emitted (for example to measure the Poynting flux in some solid angle), one might apply conservation of energy in and invert the frequency and angular distributions above to emit photons. The photons would statistically represent the radiation. Depending on the spectral and angular resolution requirements, this technique may also result in an intractable problem.

Secondary Emission of Electrons

A model for secondary emission from arbitrary surfaces with user definable coefficients has been developed and implemented in the XOOPIC code. The secondary coefficient has both angular and energy dependence, following the model of Vaughan[2]:

$$\sigma(V, \theta) = \delta_{max\,0} \left(1 + k_s \frac{\theta^2}{2\pi} \right) (w \exp(1 - w))^k,$$

9

where energy of the incident particle is denoted by V, and the angle of incidence measured from the normal is θ. Here, $\delta_{max\,0}$ is the peak in the secondary emission curve, which occurs for the incident energy $V_{max\,0}$. The parameter, k, is given by:

$$k = \begin{cases} 0.62 & w \le 1 \\ 0.25 & w > 1 \end{cases}.$$

10

The energy dependence appears implicitly in Eq. 9, through the normalized energy w:

$$w = \frac{V - V_0}{V_{max\,0}\left(1 + k_s \theta^2 / 2\pi\right) - V_0}$$

11

Here, V_0 is the threshold energy below which the secondary coefficient becomes zero (i.e. negative values of secondary coefficient are not allowed).

The angular dependence appears explicitly in the equation for the secondary coefficient as well as implicitly in the energy dependent term. The parameter, $0 \le k_s \le 2$, describes the smoothness of the surface, with 0 being rough and 2 being smooth. Vaughan uses separate smoothness factors in the angular and energy dependent parts of the equation, but says that values of 1 are recommended unless data for a specific surface supports other values.
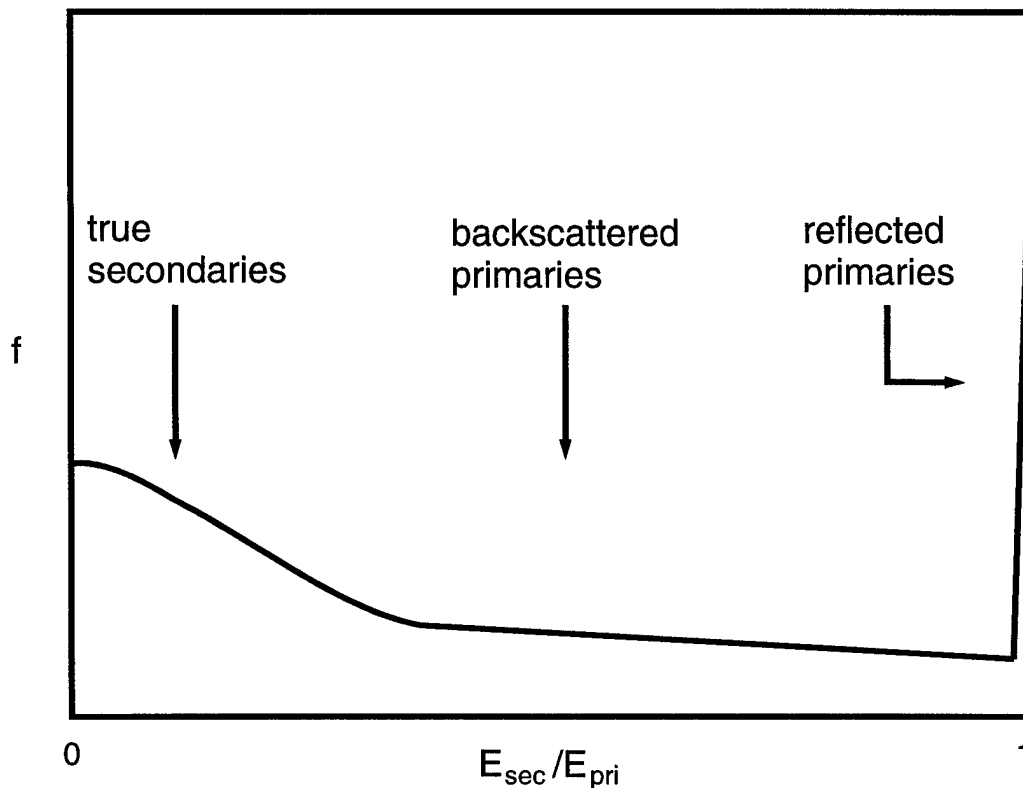

Figure 1. Secondary electron energy emission distribution

The emission spectrum of secondary electrons has three energy regimes, as shown in Figure 1. Incident electrons reflected at the surface of the secondary emitting material are called reflected primaries. Reflected primaries comprise about 3% of the emitted electron population. The energy of the reflected primary is approximately the same as the energy of the incident primary, $V_r = V_i$.

The primary is reflected specularly in angle, $\theta_r = -\theta_i$, where θ is measured from the normal to the surface of impact.

Backscattered primaries are electrons that impact the surface, and scatter off of several lattice atoms and/or impurities. Typically, backscattered primaries comprise about 7% of the emitted electron population. These electrons re-emerge from the impact surface with energies in the range $0 < V_b < V_i$. Within this energy band, all energies are taken as equally probable, $V_b = RV_i$, where $0 < R < 1$ is a uniformly distributed random number. The angle of emission is specular just as in the reflected primary case. A more detailed treatment might consider a distribution of angles resulting from quantum mechanical treatment of the lattice potentials in the secondary emission medium.

True secondaries are electrons that are emitted from the lattice at impact surface. The true secondaries comprise about 90% of the emitted electron population. Energy is imparted to the lattice electrons over some time long compared to an elastic collision time, so the electron energy distribution can be approximated as a Maxwell-Boltzmann distribution. The electrons are emitted with energies from a thermal distribution of temperature V_t,

$$f(V) = \frac{V}{V_t^2} e^{-V/V_t}.$$

12

Due to the timescale of the emission process, the angle of emission is taken to be isotropic:

$$g(\theta) = \cos(\theta)/2.$$

13

In the XOOPIC implementation, all the parameters above can be modified from the input file, with the typical values above used as defaults. The generic model can thus be used to approximately parameterize secondary emission from many different media, and indeed has been used to model electron-induced secondary emission as well as ion-induced secondary emission common to discharges. In addition, the present XOOPIC model allows for separate secondary emission treatment for each species incident on each boundary. For example, one electrode could have one profile for electrons and another for ions, while another electrode might have the same secondary emission parameters for both species.

Electromagnetic Boundary Conditions

A literature survey has been performed to acquire information about electromagnetic boundary conditions. Here we summarize the wave absorbing methods most relevant to PIC modeling, including surface impedance boundary conditions (SIBC), the Lindman EM Boundary Condition, Superabsorption Boundary Condition, and Exact Non-reflecting Boundary Conditions.

Surface impedance boundary conditions (SIBC) (see, for example, Ref.'s 3 and 6) are based on the definition of surface impedances for plane waves with horizontal or vertical polarizations. This method is employed to reduce the solution volume in the analysis of the interactions of electromagnetic waves with objects of arbitrary shape and material composition (including free space). Implementation with constant surface impedance is straightforward, but it is not accurate for waves with a large angle of incidence. This method can be expanded to include dispersive surface impedance.

The Lindman Boundary Condition is based primarily on the paper by Lindman.[4] Propagating and evanescent waves from within the computational region generates no reflected waves as they cross the Lindman boundary. The boundary condition is formulated for a wave equation. An alternate picture is to consider the boundary condition an expansion of the normal impedance boundary condition to (almost) any angle of incidence. This boundary condition is straightforward to formulate with the frequency and wavenumber domain, but is difficult to use in time and space domain code. The difficulty lies in finding a numerically efficient approximation. A disadvantage of this method is that there is a transient response to an incoming wave. The closer the incidence wave is to 90 degree incidence, the longer the transient. Another problem is that the method is unstable when there is a density jump parallel to and near the boundary, such as with a plasma sheath or beam edge.

The Superabsorption Boundary Layer can be applied to known absorbing boundary conditions, resulting in dramatic reduction in the numerical error caused by the boundary reflection. The principle and analysis of the superabsorption method is presented in Mei and Fang.[5] This method makes use of the fact that when an absorbing boundary condition is applied to the boundary electric fields, which are then used to find the magnetic fields in their neighborhood, the reflection errors in the magnetic fields are related to those magnetic fields, which are computed directly from the absorbing boundary condition. The interesting part of the relation between these two errors is that they bear the opposite sign. The results of the two different calculations of the boundary magnetic fields can be combined in such a manner that the errors cancel, but not the fields remain.

The Surface Integral Boundary Condition is an exact global method for achieving a non-reflecting boundary condition (NRBC). It is based on a time domain integral representation of the fields outside the calculation volume in terms of the known fields on the surface surrounding that volume. The robustness and accuracy of this method is countered by the complexity and large computational expense.

Let V be a volume with a surface S. The interior of V must be homogeneous and isotropic: the permittivity, ε, and permeability, μ, are constant throughout the volume. Assuming that the fields satisfy the Sommerfeld radiation condition and the source current density, $\mathbf{J}$, and charge density, ρ, are located in V, the electric field at $\mathbf{r}$ is given by:

$$\mathbf{E}(\mathbf{r},t) = \int_V dV \left(\frac{\rho(\mathbf{r}',\tau)\hat{\mathbf{R}}}{4\pi\varepsilon R^2} + \frac{\partial_t \rho(\mathbf{r}',\tau)\hat{\mathbf{R}}}{4\pi\varepsilon Rc} - \frac{\mu\partial_t \mathbf{J}(\mathbf{r}',\tau)}{4\pi R} \right)$$
$$- \oint_S \left(\frac{\hat{\mathbf{n}}\times\partial_t\mu\mathbf{H}(\mathbf{r}',\tau)}{4\pi\varepsilon R} - \frac{\hat{\mathbf{n}}\times(\mathbf{E}(\mathbf{r}',\tau)+\partial_t\mu\mathbf{E}(\mathbf{r}',\tau)\times\hat{\mathbf{R}})}{4\pi\varepsilon R^2} \right) - \frac{\hat{\mathbf{n}}\cdot(\mathbf{E}(\mathbf{r}',\tau)+\tau\partial_t\mu\mathbf{E}(\mathbf{r}',\tau)\hat{\mathbf{R}})}{4\pi\varepsilon R^2} \qquad 14$$

Where $\tau = t - R/c$, the time it takes a signal to travel from r' to r at the speed of light, $c = 1/\sqrt{\varepsilon\mu}$.

Analysis of Errors Inherent in the Generic PIC Algorithm

The errors generic PIC algorithm have been analyzed separately in the electrostatic limit by Birdsall and Langdon[6] and Hockney and Eastwood.[7] These results can be used to analyze the error in the entire PIC scheme by examining how errors can propagate from one algorithm to the

next. To demonstrate the analysis methodology, the electrostatic PIC method is examined first. Note that this step is relevant in electromagnetic schemes because the same algorithms are employed to obtain the initial fields for an initial configuration of charges. Next, the same analysis is extended to the generic electromagnetic PIC scheme.

Figure 2 shows the schematic of error propagation in the generic electrostatic PIC algorithm. Errors propagate from particle position to charge density via interpolation of PIC particle charges to the mesh. The resulting error in charge density is then propagated to the Poisson Equation. The error in potential is next propagated to the electric field as a result of the differencing scheme employed. The error in the electric field on the mesh is then propagated to the Lorentz Equations as a result of interpolation, first to particle velocity and then to the particle position. If a static magnetic field must also be interpolated from values known on a mesh, then an additional error is introduced into the Lorentz Equations. The error in the Lorentz Equations is then propagated back to the charge density and the error begins another circuit. In the following discussions, the exact value of f evaluated at x,t is written $f(x,t)$, while the discrete approximation is written f_x^t.
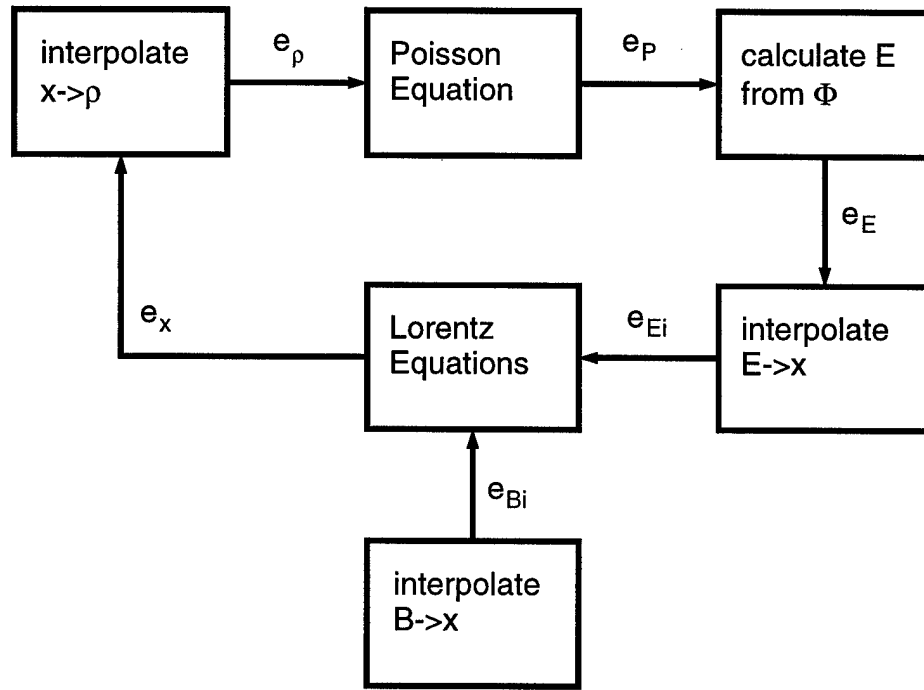

Figure 2 Electrostatic PIC error flow schematic.

First, consider the well-known error terms for the standard algorithms. The truncation error introduced by a center difference of the Poisson Equation is well known to be second order in space:

$$e_P \equiv \frac{\Phi_{x_j+\Delta x} - 2\Phi_{x_j} + \Phi_{x_j-\Delta x}}{\Delta x^2} - \nabla^2 \Phi(x) = \frac{\Delta x^2}{12} \Phi^{(4)}(x) + \frac{\Delta x^4}{360} \Phi^{(6)}(x) + O(\Delta x^6) \qquad 15$$

Similarly, the truncation error in the common leapfrog difference for the Lorentz Equations is known to be second order in time for the acceleration:

$$e_a \equiv \frac{x^{t+\Delta t} - 2x^t + x^{t-\Delta t}}{\Delta t^2} - \frac{d^2}{dt^2}x(t) = \frac{\Delta t^2}{12}x^{(4)}(t) + \frac{\Delta t^4}{360}x^{(6)}(t) + O(\Delta t^6) \qquad 16$$

It is interesting to note that the error for $x^{t+\Delta t}$ in Eq. 16 (found by solving for $x^{t+\Delta t}$) is higher order than the local error in the central difference for the velocity, given by:

$$e_v \equiv \frac{x^{t+\Delta t} - x^t}{\Delta t} - \frac{d}{dt}x(t + \Delta t/2) = \frac{\Delta t^2}{24}x^{(3)}(t + \Delta t/2) + \frac{\Delta t^4}{1920}x^{(5)}(t + \Delta t/2) + O(\Delta t^6). \qquad 17$$

This is a consequence of the cancellation of errors in the leapfrog method, and underscores the importance of proper time centering of the position and velocity. The error in position for the properly centered leap frog scheme is:

$$e_x \equiv x^{t+\Delta t} - x(t + \Delta t) = \Delta t^2 e_a. \qquad 18$$

The charge density is computed by interpolating the positions of the particles to the mesh. This error has been analyzed for a number of interpolation schemes. For nearest grid point weighting, the error in charge density is given by:

$$e_{\rho,NGP} \equiv \rho_{j,NGP} - \rho(x) = \frac{\Delta x^2}{24}\rho^{(2)}(x) + \frac{\Delta x^4}{1920}\rho^{(4)}(x) + O(\Delta x^6). \qquad 19$$

For linear weighting, the error is given by:

$$e_{\rho,lin} \equiv \rho_{j,lin} - \rho(x) = \frac{\Delta x^2}{12}\rho^{(2)}(x) + \frac{\Delta x^4}{360}\rho^{(4)}(x) + O(\Delta x^6). \qquad 20$$

It is especially illuminating to note that since $\rho^{(2)}(x) = -\varepsilon\Phi^{(4)}(x)$ by differentiating the Poisson Equation, the truncation errors in the center difference of the Poisson Equation are exactly cancelled by the error for linear weighting of charge density, **to all orders of accuracy**. Higher order weightings do not have this property; it is precisely cancellation of error that we seek in constructing these coupled algorithms, so certain methods which are lower in accuracy for one error term often cancel other errors, resulting in superior accuracy of the coupled set. We shall see below that linear weighting still introduces errors in the interpolation of electric field to particle location.

For quadratic charge interpolation, the error is given by:

$$e_{\rho,quad} \equiv \rho_{j,quad} - \rho(x) = \frac{\Delta x^2}{8}\rho^{(2)}(x) + \frac{13\Delta x^4}{16}\rho^{(4)}(x) + O(\Delta x^6). \qquad 21$$

The electric field on the mesh must be computed by finite differencing the potential on the mesh. The difference is typically a two-cell center difference, in which the error is given by:

$$e_E \equiv \frac{\Phi_{x-\Delta x} - \Phi_{x+\Delta x}}{2\Delta x} - E(x) = -\frac{\Delta x^2}{6}\Phi^{(3)}(x) + O(\Delta x^4). \qquad 22$$

The final errors to consider in the electrostatic case are the errors of interpolation of fields to particle positions. Although we only consider the electric field here, a similar exercise applies for static magnetic fields. The error for the nearest grid point interpolation is given by:

$$e_{Ei,NGP} \equiv \frac{\Phi_{x-\Delta x} - \Phi_{x+\Delta x}}{2\Delta x} - E(x + f\Delta x)$$

$$= f\Delta x \Phi^{(2)}(x + f\Delta x) - \frac{1+3f^2}{6}\Delta x^2 \Phi^{(3)}(x + f\Delta x) + O(\Delta x^3)$$

23

where $-1/2 \le f \le 1/2$ is the fraction of a cell width from a mesh on which the electric field is known. Note that NGP weighting has a first order error term.

For linear interpolation, the field interpolation error becomes:

$$e_{Ei,lin} \equiv (1-f)\frac{\Phi_{x-\Delta x} - \Phi_{x+\Delta x}}{2\Delta x} + f\frac{\Phi_x - \Phi_{x+2\Delta x}}{2\Delta x} - E(x + f\Delta x)$$

$$= \frac{3f^2 - 3f - 1}{6}\Delta x^2 \Phi^{(3)}(x + f\Delta x) + O(\Delta x^3),$$

24

where here $0 \le f \le 1$. Note that linear weighting is second order accurate.

For quadratic interpolation, the error becomes:

$$e_{Ei,quad} \equiv \frac{(1-2f)^2}{8}\frac{\Phi_{x-2\Delta x} - \Phi_x}{2\Delta x} + \left(\frac{3}{4} - f^2\right)\frac{\Phi_{x-\Delta x} - \Phi_{x+\Delta x}}{2\Delta x}$$

$$+ \frac{(1+2f)^2}{8}\frac{\Phi_x - \Phi_{x+2\Delta x}}{2\Delta x} - E(x + f\Delta x),$$

25

$$= -\frac{7 + 48f^2}{24}\Delta x^2 \Phi^{(3)}(x + f\Delta x) + O(\Delta x^3)$$

where $-1/2 \le f \le 1/2$. Note that the quadratic interpolation is second order accurate.

Next, the above analysis is extended to the fully relativistic electromagnetic PIC algorithms. The error flow schematic is shown in Figure 3. Note that the magnetic field is often solved in parts (Faraday box) by advancing exactly ½ to get to a time level t for use in the particle interpolation. The remaining half advance is performed just prior to the Ampere box. It is useful to note that although several parts of the diagram have multiple branches, many of the error terms are identical to the electrostatic case. The interpolation of fields to particle locations is unchanged from the preceding analysis (although the locations may change by half cells to accommodate the Yee mesh or an additional averaging of fields to nodes, shown above, may be more efficient). The analysis for the Lorentz Equations is also still valid, with the velocity v replaced by the normalized momentum, $u = \gamma v$. An initial analysis of the acceleration error indicates the leading term is second order in Δt, and is also proportional to γ^6.
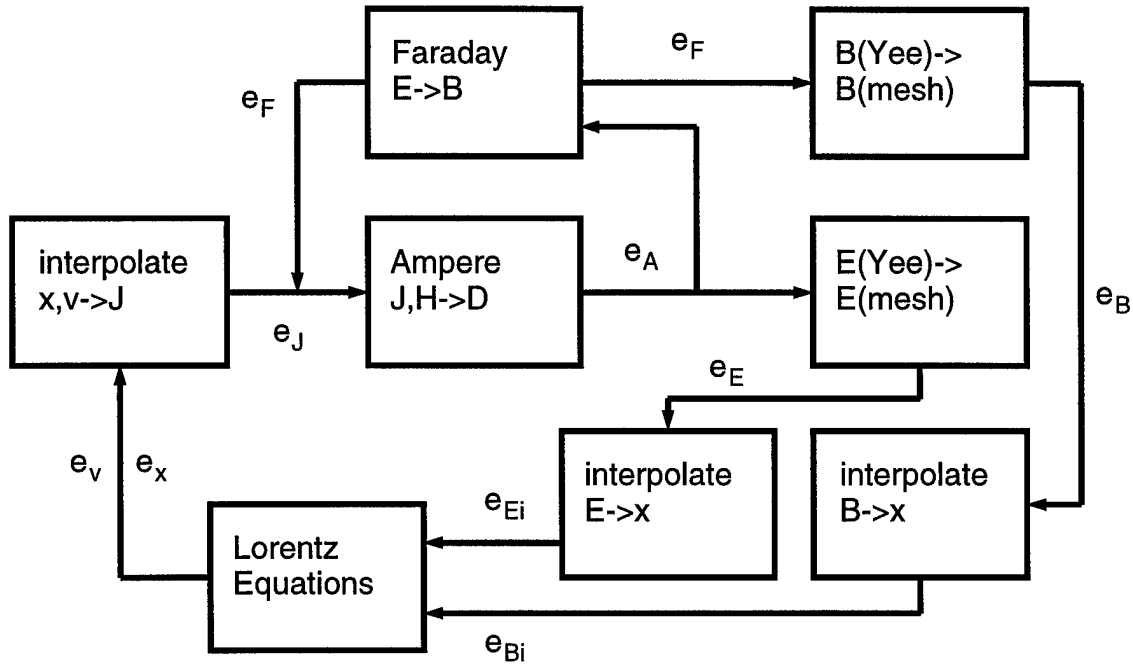
Figure 3. Electromagnetic PIC error flow schematic.

In addition to the divergence equations examined above, we must now consider the Maxwell curl equations. The field components are defined in the usual way, with locations as shown in Figure 4. Note that the current density is co-located with the electric field. The error in Faraday's Law can be written:

$$
e_F \equiv \frac{\mathbf{B}^{t+\Delta t/2} - \mathbf{B}^{t-\Delta t/2}}{\Delta t} - \frac{\partial}{\partial t}\mathbf{B}\left(t, \mathbf{x} + \frac{\Delta \mathbf{x}}{2}\right) + \begin{pmatrix} \dfrac{E_{z,y+\Delta y} - E_{z,y}}{\Delta y} - \dfrac{E_{y,z+\Delta z} - E_{y,z}}{\Delta z} \\[2mm] \dfrac{E_{x,z+\Delta z} - E_{x,z}}{\Delta z} - \dfrac{E_{z,x+\Delta x} - E_{z,x}}{\Delta x} \\[2mm] \dfrac{E_{y,x+\Delta x} - E_{y,x}}{\Delta x} - \dfrac{E_{x,y+\Delta y} - E_{x,y}}{\Delta y} \end{pmatrix}^t - \nabla\times\mathbf{E}\left(t, \mathbf{x} + \frac{\Delta \mathbf{x}}{2}\right)
$$

$$
= \frac{\Delta t^2}{24}\mathbf{B}^{(3)}\left(t, \mathbf{x} + \frac{\Delta \mathbf{x}}{2}\right) + \frac{1}{24}\begin{pmatrix} \Delta y^2 \dfrac{\partial^3 E_z(t, \mathbf{x} + \Delta \mathbf{x}/2)}{\partial y^3} - \Delta z^2 \dfrac{\partial^3 E_y(t, \mathbf{x} + \Delta \mathbf{x}/2)}{\partial z^3} \\[2mm] \Delta z^2 \dfrac{\partial^3 E_x(t, \mathbf{x} + \Delta \mathbf{x}/2)}{\partial z^3} - \Delta x^2 \dfrac{\partial^3 E_z(t, \mathbf{x} + \Delta \mathbf{x}/2)}{\partial x^3} \\[2mm] \Delta x^2 \dfrac{\partial^3 E_y(t, \mathbf{x} + \Delta \mathbf{x}/2)}{\partial x^3} - \Delta y^2 \dfrac{\partial^3 E_x(t, \mathbf{x} + \Delta \mathbf{x}/2)}{\partial y^3} \end{pmatrix}
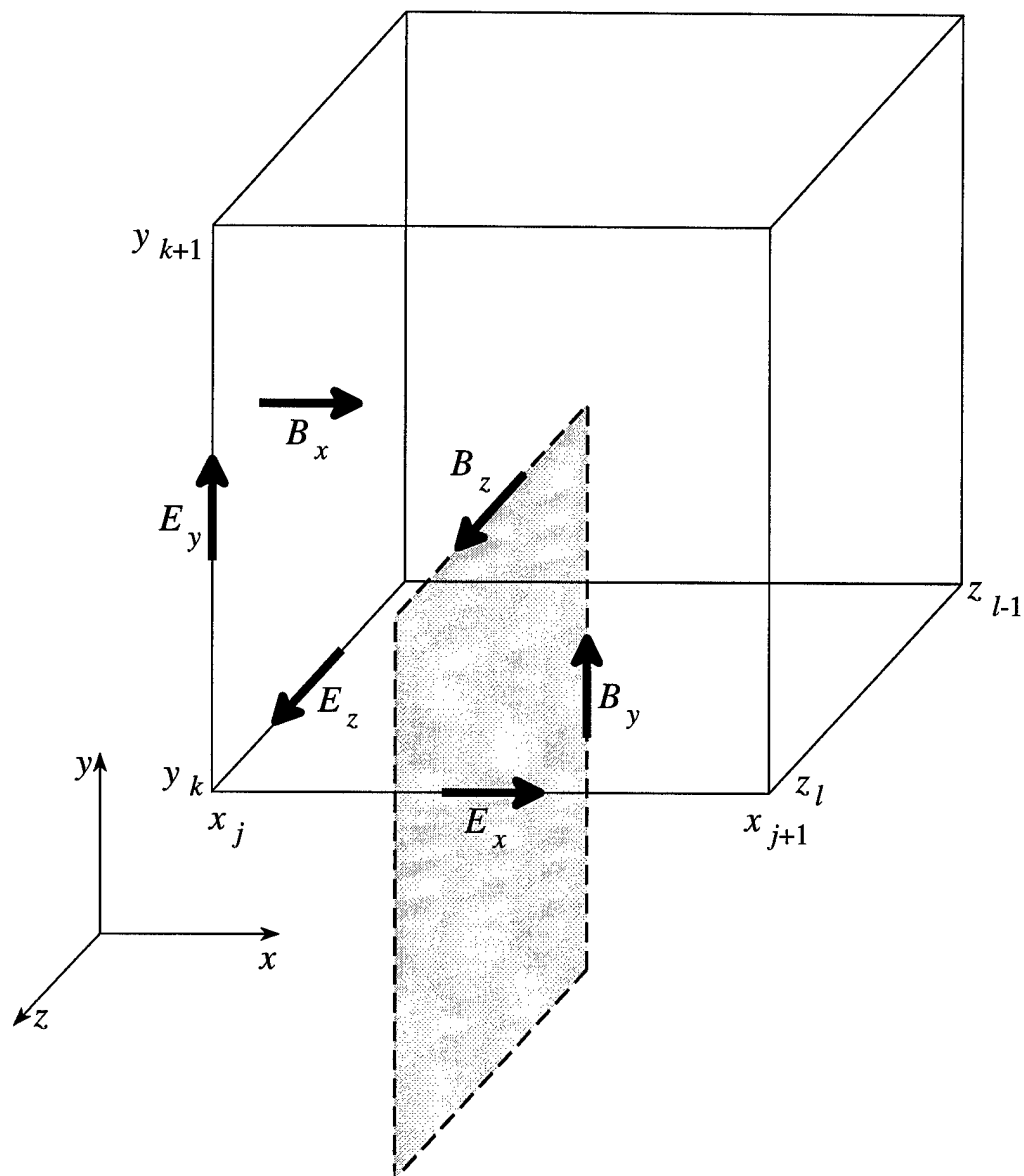$$

26

Figure 4. Location of fields on the standard Yee mesh.

Similarly, the error in Ampere's Law can be written:

$$e_F \equiv \frac{\mathbf{D}^{t+\Delta t} - \mathbf{D}^t}{\Delta t} - \frac{\partial}{\partial t}\mathbf{D}\left(t,\mathbf{x}+\frac{\Delta \mathbf{x}}{2}\right) - \left(\begin{array}{cc} \dfrac{H_{z,y+\Delta y} - H_{z,y}}{\Delta y} - \dfrac{H_{y,z+\Delta z} - H_{y,z}}{\Delta z} \\ \dfrac{H_{x,z+\Delta z} - H_{x,z}}{\Delta z} - \dfrac{H_{z,x+\Delta x} - H_{z,x}}{\Delta x} \\ \dfrac{H_{y,x+\Delta x} - H_{y,x}}{\Delta x} - \dfrac{H_{x,y+\Delta y} - H_{x,y}}{\Delta y} \end{array}\right)^t + \nabla \times \mathbf{H}\left(t,\mathbf{x}+\frac{\Delta \mathbf{x}}{2}\right)$$

$$= \frac{\Delta t^2}{24}\mathbf{D}^{(3)}\left(t,\mathbf{x}+\frac{\Delta \mathbf{x}}{2}\right) + \frac{1}{24}\left(\begin{array}{c} \Delta y^2 \dfrac{\partial^3 H_z(t,\mathbf{x}+\Delta \mathbf{x}/2)}{\partial y^3} - \Delta z^2 \dfrac{\partial^3 H_y(t,\mathbf{x}+\Delta \mathbf{x}/2)}{\partial z^3} \\ \Delta z^2 \dfrac{\partial^3 H_x(t,\mathbf{x}+\Delta \mathbf{x}/2)}{\partial z^3} - \Delta x^2 \dfrac{\partial^3 H_z(t,\mathbf{x}+\Delta \mathbf{x}/2)}{\partial x^3} \\ \Delta x^2 \dfrac{\partial^3 H_y(t,\mathbf{x}+\Delta \mathbf{x}/2)}{\partial x^3} - \Delta y^2 \dfrac{\partial^3 H_x(t,\mathbf{x}+\Delta \mathbf{x}/2)}{\partial y^3} \end{array}\right)$$

27

The positions of the analytic terms, including the derivatives, in Eqs. 26-27 are at the Yee mesh locations as per Figure 4. Both curl equations are second order in space and time.

The final error term to consider involves weighting the current to the mesh for the source term to the Maxwell Equations. For symmetric current weightings, such as nearest grid point in all directions, charge is not conserved on the mesh assuming a symmetric charge density weighting. Charge dipoles grow in time for such a weighting, leading to catastrophic failure; methods exist to reduce this problem[8]. The errors for symmetric current weightings are identical to the charge density weighting of the same type. In charge conserving current weighting schemes, the order of the interpolation in the direction of the current component is one order lower than the transverse interpolation. Here, we will only analyze the error for the NGP-linear current weighting:

$$e_{J1} \equiv J_{x,x+\Delta x/2} - J_x(x+\Delta x/2) = \frac{\Delta y^2}{12}J_x^{(0,2)}(x+\Delta x/2) + \frac{\Delta x \Delta y^2}{24}J_x^{(1,2)}(x+\Delta x/2)$$
$$+ \frac{\Delta x^2}{72}\left(3J_x^{(2,0)}(x+\Delta x/2) + \Delta y^2 J_x^{(2,2)}(x+\Delta x/2)\right) + O(\Delta x^3) \quad ; \qquad 28$$

$$e_{J2} \equiv J_{y,y+\Delta y/2} - J_y(y+\Delta y/2) = \frac{\Delta x^2}{12}J_y^{(2,0)}(y+\Delta y/2) + \frac{\Delta y \Delta x^2}{24}J_y^{(2,1)}(x+\Delta x/2)$$
$$+ \frac{\Delta y^2}{72}\left(3J_y^{(0,2)}(y+\Delta y/2) + \Delta x^2 J_y^{(2,2)}(y+\Delta y/2)\right) + O(\Delta x^3) \qquad . \qquad 29$$

The above error analysis demonstrates that despite incomplete analysis in the literature, it is possible to write truncation error terms for each component of the standard PIC method in both the electrostatic and electromagnetic limits. We believe this analysis is an invaluable contribution to the existing body of knowledge, which provides a theoretical basis for the PIC algorithms and method as a whole.

A large subset of the existing XOOPIC GUI, which runs only under Unix, has been ported to a new cross-platform windowing library, called Qt,[9] that runs equally well on Microsoft Windows 95/98/NT and all versions of Unix. Figure 5 shows a screen capture of the new GUI running a klystron simulation on a PC. The Run/Stop, Step and Open/Close Diagnostics buttons on the main control panel (seen in the upper left of Figure 5) have been implemented.
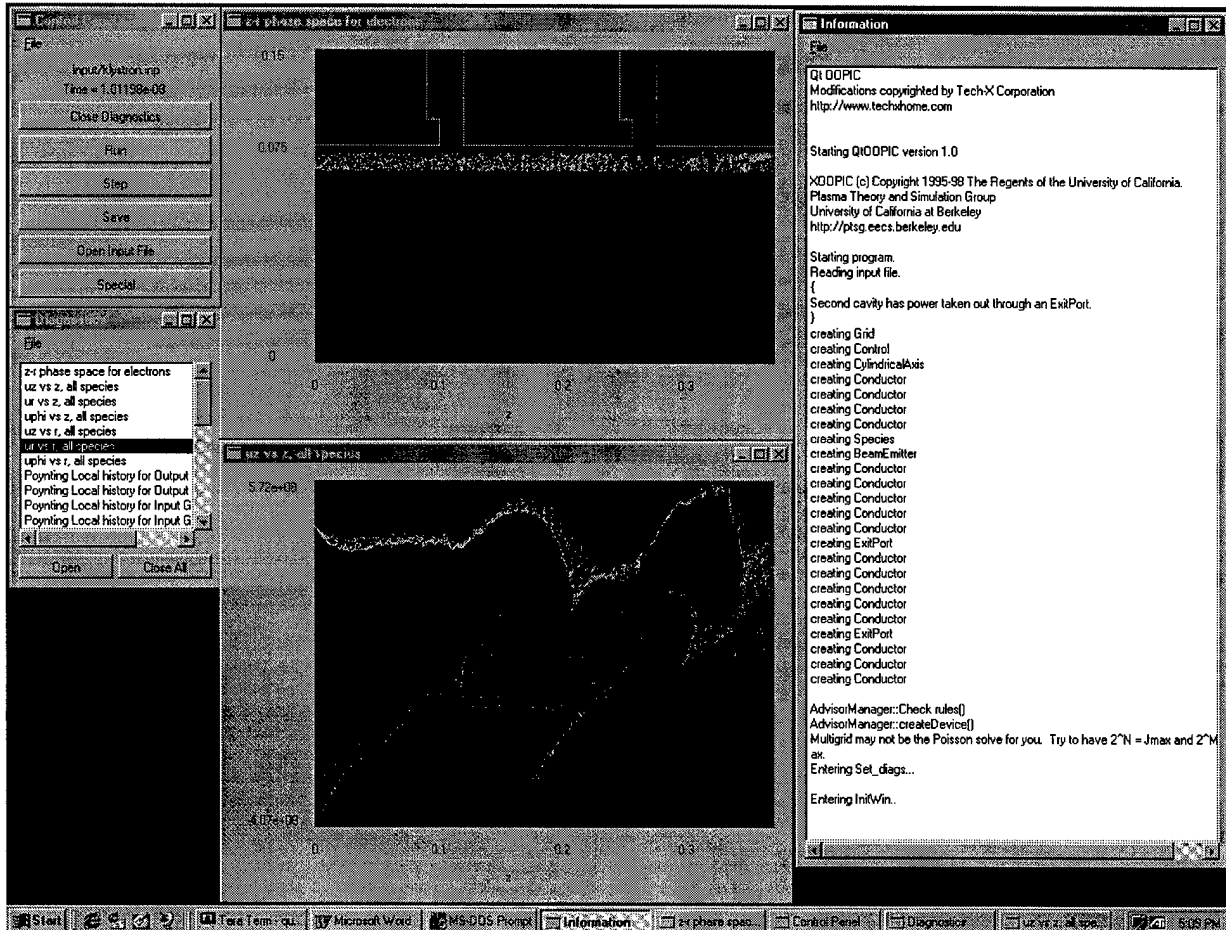

Figure 5. OOPIC simulation of a klystron with cylindrical symmetry, running under Windows 98. Control and diagnostic windows are on the left; top center shows metal structures in the z-r plane and electrons streaming in the z-direction; bottom center shows bunching of electrons in z-pz phase space; messages from the code appear in the window on the right.

The 3-D plots of the existing XOOPIC GUI have been reimplemented in the new cross-platform prototype using the Qt library's direct support for OpenGL,[10] which is now the standard for interactive 3-D computer graphics. Figure 6 shows a screen capture of the new GUI running a simulation of electrons streaming into a cylindrical can and ionizing neutral Argon. The two lower right windows show 3-D surface plots generated with OpenGL. The first three sliders along the left side of these windows allow the user to rotate the plot about the three axes, while the fourth slider zooms the image in and out. Axis labels, color effects and other features have

not yet been added. The prototype executable that is available from the Tech-X web site does not include the OpenGL graphics, because these have not been tested as thoroughly as the 2-D plots.
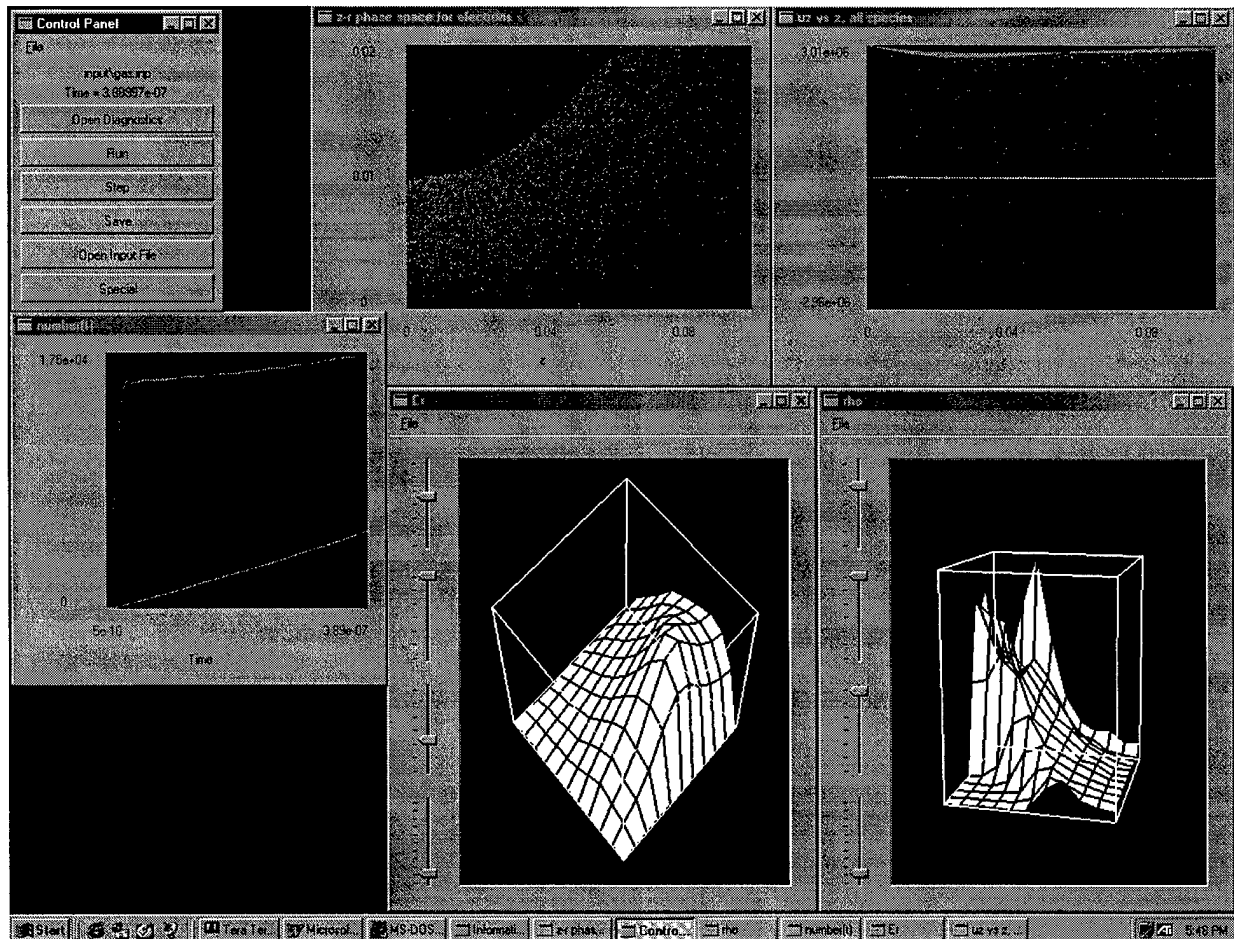

Figure 6. OOPIC simulation of electrons streaming into a cylindrical can of Argon, including collisional ionization. Top center shows electron beam in the z-r plane, expanding radially due to space charge forces; top right shows z-pz phase space, with streaming electrons along the top, cold ions along the pz=0 axis, and scattered electrons throughout; center left shows the number of electrons (top line) and ions (bottom line) in the simulation; bottom center shows OpenGL surface plot of the radial electric field component in the z-r plane; bottom right shows OpenGL surface plot of the total particle density

This prototype cross-platform GUI has been tested successfully on PC's running Microsoft Windows 95 and 98 and NT, as well as on the following Unix platforms: a SunUltra5 running Solaris, a Pentium Pro PC running linux, a DecAlpha running linux and an SGI running Irix. We have established a truly cross-platform development environment, which allows us to further develop the GUI on any PC or any Unix computer, then recompile the changes on all other platforms with no difficulty.

1   J. D. Jackson, *Classical Electrodynamics*, John Wiley and Sons (1975).

2   J. R. M. Vaughan, IEEE Trans. Electron Devices **ED-36**, 1963 (1989).

3   J. P. Verboncoeur, M. V. Alves, V. Vahedi, and C. K. Birdsall, "Simultaneous potential and circuit solution for 1d bounded plasma particle simulation codes", *Journal of Computational Physics* **104**, 321-328 (1993).

4   E. L. Lindman, "Free space boundary conditions for the time-dependent wave equation", J. Comp. Phys. **18**, 66-78 (1975).

5   K. K. Mei and J. Fang, "Superabsorption – a method to improve absorbing boundary conditions (electromagnetic waves)", IEEE Tran. Ant. And Prop. **40**, 1001-1010 (1992).

6   C. K. Birdsall and A. B. Langdon, *Plasma Physics via Computer Simulation*, McGraw-Hill, New York, N.Y. (1985).

7   R. W. Hockney and J. W. Eastwood, *Computer Simulation Using Particles*, McGraw-Hill, New York, N.Y. (1981).

8   P. J. Mardahl and J. P. Verboncoeur, "Charge conservation in electromagnetic PIC codes; spectral comparison of Boris/DADI and Langdon-Marder methods", Comp. Phys. Comm. 106, 219-229 (1997).

9   Troll Tech; Qt home page at URL http://www.troll.no

10   OpenGL home page at URL http://www.opengl.org